NIR-II/NIR-I Fluorescence Molecular Tomography of Heterogeneous Mice Based on Gaussian Weighted Neighborhood Fused Lasso Method

Meishan Cai, Zeyu Zhang, Xiaojing Shi, Zhenhua Hu, and Jie Tian, *Fellow, IEEE*

***Abstract*— Fluorescence molecular tomography (FMT), which can visualize the distribution of fluorescence biomarkers, has become a novel three-dimensional noninvasive imaging technique for *in vivo* studies such as tumor detection and lymph node location. However, it remains a challenging problem to achieve satisfactory reconstruction performance of conventional FMT in the first near-infrared window (NIR-I, 700-900nm) because of the severe scattering of NIR-I light. In this study, a promising FMT method for heterogeneous mice was proposed to improve the reconstruction accuracy using the second near-infrared window (NIR-II, 1000-1700nm), where the light scattering significantly reduced compared with NIR-I. The optical properties of NIR-II were analyzed to construct the forward model for NIR-II FMT. Furthermore, to raise the accuracy of solution of the inverse problem, we proposed a novel Gaussian weighted neighborhood fused Lasso (GWNFL) method. Numerical simulation was performed to demonstrate the outperformance of GWNFL compared with other algorithms. Besides, a novel NIR-II/NIR-I dual-modality FMT system was developed to contrast the *in vivo* reconstruction performance between NIR-II FMT and NIR-I FMT. To compare the reconstruction performance of NIR-II FMT with traditional NIR-I FMT, numerical simulations and *in vivo* experiments were conducted. Both the simulation and *in vivo* results showed that NIR-II FMT outperformed NIR-I FMT in terms of location accuracy and spatial overlap index. It is believed that this study could promote the development and biomedical application of NIR-II FMT in the future.**

***Index Terms*— Fluorescence molecular tomography, NIR-II, NIR-I, GWNFL method.**

Manuscript received November 11, 2019; revised December 26, 2019; accepted January 3, 2020. Date of publication January 17, 2020; date of current version June 1, 2020. This work was supported in part by the National Key Research and Development Program of China under Grant 2017YFA0205200 and Grant 2016YFC0102600, in part by the National Natural Science Foundation of China (NSFC) under Grant 81930053, Grant 61622117, Grant 81671759, and Grant 81227901, in part by the Beijing Natural Science Foundation under Grant JQ19027, in part by the Beijing Nova Program under Grant Z181100006218046, in part by the Scientific Instrument Developing Project of the Chinese Academy of Sciences under Grant YZ201672, in part by the Chinese Academy of Sciences under Grant GJJSTD20170004, in part by the Key Research Program of the Chinese Academy of Sciences under Grant KGZD-EW-T03, and in part by the Innovative Research Team of High-Level Local Universities in Shanghai. *(Corresponding authors: Zhenhua Hu; Jie Tian.)*

Meishan Cai and Xiaojing Shi are with the CAS Key Laboratory of Molecular Imaging, Institute of Automation, Beijing 100190, China, and also with the School of Artificial Intelligence, University of Chinese Academy of Sciences, Beijing 100049, China (e-mail: cameishan2016@ia.ac.cn; shixiaojing2017@ia.ac.cn).

Zeyu Zhang is with the CAS Key Laboratory of Molecular Imaging, Institute of Automation, Beijing 100190, China, and also with the School of Life Science and Technology, Xidian University, Xi'an 710071, China (e-mail: zhang.zey.doc@gmail.com).

Zhenhua Hu is with the CAS Key Laboratory of Molecular Imaging, Institute of Automation, Beijing 100190, China, also with the School of Artificial Intelligence, University of Chinese Academy of Sciences, Beijing 100049, China, and also with the Beijing Key Laboratory of Molecular Imaging, Beijing 100190, China (e-mail: zhenhua.hu@ia.ac.cn).

Jie Tian is with the CAS Key Laboratory of Molecular Imaging, Institute of Automation, Beijing 100190, China, also with the Beijing Key Laboratory of Molecular Imaging, Beijing 100190, China, and also with the Beijing Advanced Innovation Center for Big Data-Based Precision Medicine, Beihang University, Beijing 100191, China (e-mail: tian@ieee.org).

This article has supplementary downloadable material available at http://ieeexplore.ieee.org, provided by the authors.

Color versions of one or more of the figures in this article are available online at http://ieeexplore.ieee.org.

Digital Object Identifier 10.1109/TMI.2020.2964853

I. Introduction

FLUORESCENCE molecular imaging (FMI) in the near-infrared (NIR) region has been widely used in preclinical research and clinical practice for its high spatial and temporal resolutions [1]–[3]. Based on the optical signal excited from the fluorescent dyes, FMI has become an effective and significant technique for tumor detection, image-guided surgery, lymph node visualization, and other biomedical applications [4], [5]. Compared with other optical molecular imaging modalities, such as bioluminescence imaging (BLI) [6] and Cherenkov luminescence imaging (CLI) [7], FMI has a better prospect for clinical translation because of high penetration depth, operation convenience, non-radiation, and low cost.

Over the past decades, the first NIR window (NIR-I, 700-900 nm) is the mainly adopted imaging spectrum for FMI (NIR-I FMI) owing to the emerging NIR-I dyes [2]. However, NIR-I FMI can only achieve a planar image, which is incapable of determining the exact location of tumors *in vivo* because of the lack of depth information [8]. To overcome the defects of FMI, fluorescence molecular tomography in the first NIR window (NIR-I FMT) is developed to detect the three-dimensional (3D) distribution of fluorescent dyes [9]. Based on the combination of the NIR-I FMI information and the anatomical information such

as computed tomography (CT) [10] and magnetic resonance imaging (MRI) [11], NIR-I FMT has been fully developed for preclinical diagnosis and small animal experiments [12], [13]. However, NIR-I FMT is still severely ill-posed and ill-conditioned owning to the strong scattering of NIR-I light in the biological tissues [14].

To solve this problem for enhancing the performance of FMT, many strategies have been explored. Typically, fluorescence images at different angles are acquired and fused with anatomical images to reduce the ill-posedness of the inverse problem [15]. The regularization method is another useful technique for controlling the ill-posedness such as iterative shrinkage with L1-norm regularization [16], Tikhonov regularization [17], nonconvex regularization [18], and joint L1 and total variation regularization [19]. Another significant approach is to alleviate the light scattering effect exemplified as early-photon technology [20].

Fluorescence molecular imaging in the second near-infrared window (1000-1700 nm, NIR-II FMI), as a novel imaging technology, has attracted much attention in recent years. Recent advancements demonstrate that NIR-II imaging has deeper tissue penetration depth (up to centimeter-level) and higher spatial resolution than NIR-I imaging, mainly due to the reduced tissue scattering effect and the minimal autofluorescence resulting from the longer wavelength [21]–[24]. Therefore, the light in the NIR-II window can be used for FMT (NIR-II FMT) to further enhance the reconstruction accuracy and spatial overlap. On the other hand, the lack of effective and clinically available dyes limits the clinical applications of NIR-II imaging [25]. Recent studies have reported that indocyanine green (ICG) emits tail fluorescence in the NIR-II window and is suitable for NIR-II FMI [26]–[28]. These advancements have promoted the development of NIR-II imaging and created favorable conditions for NIR-II FMT.

Recently, Yang et al. carried out a preliminary study of NIR-II FMT using a homogeneous slab-shaped phantom of 1% Intralipid [29]. However, there still exist some problems that need to be solved for the NIR-II FMT of the real, optically heterogeneous mice. First, the optical properties of different tissues in the NIR-II window remain unknown, which leads to the inability to achieve the forward model accurately. Furthermore, the inverse problem of NIR-II FMT was roughly solved with the Tikhonov regularization method, which was inaccurate and over-smoothed. As the inverse problem is independent of the wavelength, traditional methods such as iterative shrinkage with L1-norm (IS_L1), joint L1 and TV (L1_TV) in NIR-I FMT can be used in NIR-II FMT. However, all these existing methods all have some defects, and they are unable to solve the inverse problem in NIR-II/NIR-I FMT accurately. Therefore, a novel method is required to obtain a more accurate solution of the inverse problem. In addition, the tomography system of NIR-II FMT is currently absent for *in vivo* experiments.

In this study, the optical properties of NIR-II light and NIR-I light in different tissues were analyzed using empirical formulas and cubic B-spline fitting method to construct the forward model. Then, a novel Gaussian weighted neighborhood fused Lasso (GWNFL) method was proposed to obtain the accurate solution of the inverse problem in NIR-II/NIR-I FMT. The reconstruction performance of GWNFL was fully verified in numerical simulation compared with Tikhonov regularization, IS_L1, L1_TV and non-Gaussian weighted neighborhood fused Lasso (NGWNFL). Besides that, a novel NIR-II/NIR-I dual-modality FMT system was established for *in vivo* NIR-II FMT and NIR-I FMT simultaneously. Numerical simulations and *in vivo* experiments were designed to verify the reconstruction performance of NIR-II FMT.

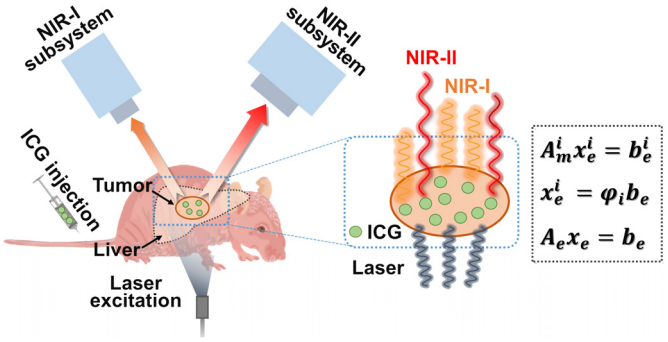

Fig. 1. The three stages of the propagation process of NIR-II/NIR-I light.

II. Methodology

A. Light Propagation Model

For continuous wave FMT, the entire light propagation process can be divided into three stages (Fig. 1). In stage 1, the excitation light transports from the body surface to the tumor area with accumulated fluorescent dyes such as ICG and Methylene Blue (MB). In stage 2, the excitation light distributed in the tumor area is converted into longer-wavelength emission light through the fluorescent dyes. In stage 3, the emission light passes through the biological tissues and reaches the body surface, detected by the charge coupled devices (CCDs). There exist strong tissue attenuation and light scattering in stages 1 and 3, which leads to the attenuation and blurring of the fluorescence signals. For FMT, the distribution of the fluorescence yield needs to be reconstructed according to the fluorescence molecular images and anatomical images.

Without considering the time effect, the excitation and emission light propagation is approximately depicted using the diffusion equation (DE). For FMT, the propagation process of excitation and emission light is formulated as coupled diffusion equations with the Robin boundary condition [30]

$$\begin{cases} \nabla\left[D_x\left(r\right)\nabla\Phi_x\left(r\right)\right]-\mu_{ax}\Phi_x\left(r\right)=-\Theta\delta\left(r-r_l\right), r\in\Omega \\ \nabla\left[D_m\left(r\right)\nabla\Phi_m\left(r\right)\right]-\mu_{am}\Phi_m\left(r\right) \\ \qquad\qquad =-\Phi_x\left(r\right)\eta\mu_{af}\left(r\right), r\in\Omega \\ 2D_{x,m}\left(r\right)\nabla\Phi_{x,m}\left(r\right)+\upsilon\Phi_{x,m}\left(r\right)=0, r\in\partial\Omega \end{cases} \tag{1}$$

where x and m denote the excitation light and emission light, respectively; $\Phi_{x,m}(r)$ is the photon flux density at the position r inside the image region Ω; $\mu_{am,ax}$ is the absorption coefficient, $\mu_{sm,sx}$ is the scattering coefficient, g is the anisotropy coefficient, $D_{x,m}=1/\left[3\mu_{am,ax}+3(1-g)\mu_{sm,sx}\right]$ is the diffusion coefficient; r_l and Θ denote the position and amplitude

of the excitation point light source, respectively; $\eta\mu_{af}(r)$ represents the fluorescent yield required to be reconstructed in the inverse problem of FMT, and υ denotes the optical reflective index of the biological tissues. By utilizing the finite element method (FEM) to discretize the light propagation model, the partial differential Eq. (1) is linearized into a system of linear equations as follows

$$\begin{cases} M_x \Phi_x = S_x \\ M_m \Phi_m = GX \end{cases} \tag{2}$$

where Φ_x and Φ_m are the density distributions of the excitation light and the emission light, respectively. M_x and M_m represent the forward system matrices of the light propagation processes. S_x denotes the distribution of the discretized excitation point source usually assumed to be the one-hot vector. G is obtained at the discretized process of fluorescent yield according to the excitation light Φ_x. X is the distribution of fluorescent yield that needs to be solved for FMT. Finally, the linear relationship between the emission light distribution Φ_m and the unknown fluorescence yield distribution X is described as

$$\Phi_m = M_m^{-1} GX = AX \tag{3}$$

where $A = M_m^{-1} G$ is the final system matrix of FMT. Since only partial nodes can be detected by the CCD, the unmeasured nodes are removed from Φ_m and the corresponding rows are removed from A as

$$\Phi_m^s = A^s X \tag{4}$$

where Φ_m^s is the measured emission light distribution, A^s is the corresponding system matrix. Therefore, the inverse problem of FMT is to solve fluorescent yield distribution X in Eq. (4).

B. Optical Properties Analysis

As shown in Eq. (1), the optical properties of biological tissues need to be obtained to establish the light propagation model. Owing to the lack of optical properties in the NIR-II spectrum window, the study of NIR-II FMT has been hampered. Here, a numerical analysis method was proposed to obtain the optical properties both in the NIR-I and NIR-II windows. The optical properties depend on the composition of different tissues r and the wavelength of photons λ for the heterogeneous mice model. Since absorption is mainly derived from oxy-hemoglobin, hypoxic hemoglobin, and water, the absorption coefficient $\mu_a(r, \lambda)$ is approximately equal to the weighted sum of the absorption coefficients of the three components [31]

$$\mu_a(\lambda) = A(\delta\mu_1(\lambda) + (1-\delta)\mu_2(\lambda)) + B\mu_3(\lambda) \tag{5}$$

where A, B, and δ are the empirical parameters dependent on the different organs, which are given in related works [31], [32]. $\mu_1(\lambda)$, $\mu_2(\lambda)$, and $\mu_3(\lambda)$ are the absorption coefficients of the oxy-hemoglobin, hypoxic hemoglobin, and water, respectively. $\mu_3(\lambda)$ at the wavelength from 690 nm to 2630 nm, and $\mu_1(\lambda)$ and $\mu_2(\lambda)$ at the wavelength from 400 nm to 1000 nm are given in related works [33], [34]. Cubic B-spline fitting is employed to calculate $\mu_1(\lambda)$ and $\mu_2(\lambda)$ in the NIR-II region with the value in the NIR-I region. Reduced scattering coefficient $\mu_s'(r, \lambda) = (1-g)\mu_s(r, \lambda)$ is calculated by the empirical formula [34]

$$\mu_s'(r, \lambda) = a \times \lambda^{-b} \tag{6}$$

where a and b are the empirical parameters dependent on the tissues [31]. The anisotropy coefficient $g(r, \lambda)$ changes little with the wavelength, and thus, it is set to an empirical constant [35].

C. Gaussian Weighted Neighborhood Fused Lasso Method

1) Constructing the Objective Optimization Function: The inverse problem of FMT is to solve Eq. (4) to calculate the density of the fluorescence yield distribution. Because of the limitation of measurement, the length of row of A^s is much less than the column size, which leads to the great ill-posedness of FMT. To obtain an accurate and robust reconstruction of FMT, different types of regularization methods with corresponding prior information have been suggested. The overall problem for solving FMT with regularization method can be written as

$$\tilde{X} = \arg min_X (f_L(X) + f_R(X)) \tag{7}$$

where $f_L(X) = \frac{1}{2}\left\|A^s X - \Phi_m^s\right\|^2$ is the least square loss function, and $f_R(X)$ is the regularization term. By using the sparse prior of fluorescent distribution, the L1-norm regularization is adopted as $f_R(X) = \lambda\|X\|_1$, which is widely known as the Lasso method. However, the Lasso method only utilizes the sparsity of the fluorescent signal, ignoring the structure information, which may lose the edge information due to the over-sparsity. A fused Lasso can obtain a more accurate reconstruction result by adding the local correlation prior to the basis of the sparse prior. The local correlation can usually be expressed as [19]

$$f_C(X) = \lambda\|\nabla X\|_1 = \lambda\sum_i |X_i - X_{i-1}| \tag{8}$$

Therefore, the regularization term of fused Lasso can be written as [36]

$$\begin{aligned} f_R(X) &= \lambda_1\|X\|_1 + \lambda_2\|\nabla X\|_1 \\ &= \lambda_1\sum_i X_i + \lambda_2\sum_i |X_i - X_{i-1}| \end{aligned} \tag{9}$$

However, only the local correlation between a node and its nearest node has been considered, which is still not sufficiently accurate and stable because of the inadequate local information. In this paper, a novel GWNFL method is proposed that can provide the local correlation between a node and its k-nearest neighbors in FMT. The GWNFL assumes that the fluorescence energy of a node is related to its k-nearest neighbors and the correlation decreases with an increase in the Euclidean distance. The Gaussian weight derived from the Euclidean distance reflects the correlation size. For GWNFL, the k nearest neighbors of node i are put into the neighbor set

firstly. Then, the Gaussian weights are calculated as

$$w_{i,j} = exp\left(-\frac{d_{i,j}^2}{4R^2}\right)/S_i$$
$$S_i = \sum\nolimits_j exp\left(-\frac{d_{i,j}^2}{4R^2}\right)$$
$$i = 1, 2, \cdots, n;\ j = 1, 2, \cdots, k \tag{10}$$

where n is the number of nodes that need to be reconstructed and R is the kernel radius to control the decay rate. R is set as a constant for both imaging modalities, and it does not depend on the tissue type. $d_{i,j} = \sqrt{\left(x_i - x_{t_j}\right)^2 + \left(y_i - y_{t_j}\right)^2 + \left(z_i - z_{t_j}\right)^2}$ is the Euclidean distance between nodes i and its j nearest neighbor. If the Gaussian distance is not used as the weight, all neighbors will have the same correlation, referred to as the NGWNFL method. Therefore, the correlation regularization term can be written as

$$f_C(X) = \lambda \left\| L_C X \right\|_1 \tag{11}$$

where L_C is the correlation matrix defined as:

$$L_C = \left(-l_{p,q}\right)_{n\times n} \tag{12}$$

$$l_{p,q} = \begin{cases} -\sum_{r\neq p} l_{p,r}, & p = q \\ w_{p,j}, & q\ is\ the\ j-nearest\ neighbor\ of\ q \\ 0, & otherwise \end{cases} \tag{13}$$

Therefore, the objective optimization function of GWNFL can be written as

$$f(x) = \frac{1}{2}\left\| A^s X - \Phi_m^s \right\|^2 + \lambda_1 \left\| X \right\|_1 + \lambda_2 \left\| L_C X \right\|_1 \tag{14}$$

2) Solving the GWNFL: Eq. (14) is a convex but non-differentiable function, which cannot be solved by the traditional gradient-based optimization method. The split Bregman method is usually used to solve this type of optimization problem. A simple derivation process for solving the GWNFL objective function is given in this paper, and more details can be found in related works [37], [38]. The unconstrained optimization problem (14) can be reformulated into an equivalent constrained problem as [39]

$$\begin{aligned} &min_X E(X) + \lambda_1 \left\| a \right\|_1 + \lambda_2 \left\| b \right\|_1 \\ &s.t.\ a = X \\ &\quad b = L_C X \end{aligned} \tag{15}$$

where $E(X) = \frac{1}{2}\left\| A^s X - \Phi_m^s \right\|^2$ is the mean square loss function. The Lagrangian function of the equation can be constructed as

$$\begin{aligned} \mathfrak{L}(X, a, b, u, v) = E(X) + \lambda_1 \left\| a \right\|_1 + \lambda_2 \left\| b \right\|_1 \\ + \langle u, a - X \rangle + \langle v, b - L_C X \rangle \end{aligned} \tag{16}$$

where u and v are the dual variables corresponding to the linear constraints. The augmented Lagrangian function of equation is

$$\begin{aligned} \mathcal{L}(X, a, b, u, v) = E(X) + \lambda_1 \left\| a \right\|_1 + \lambda_2 \left\| b \right\|_1 + \langle u, a - X \rangle \\ + \langle v, b - L_C X \rangle + \frac{\mu_1}{2}\left\| a - X \right\|_2^2 \\ + \frac{\mu_2}{2}\left\| b - L_C X \right\|_2^2 \end{aligned} \tag{17}$$

where $\mu_1 > 0$ and $\mu_2 > 0$ need to be set. The saddle point problem can be solved by optimizing the primal problem and the dual problem alternately as

$$\begin{aligned} &Primal\ problem: X^{k+1}, a^{k+1}, b^{k+1} \\ &\quad = \arg\min \mathcal{L}\left(X, a, b, u^k, v^k\right) \\ &Dual\ problem: u^{k+1} \\ &\quad = u^k + \delta_1\left(a^{k+1} - X^{k+1}\right) \\ &v^{k+1} \\ &\quad = v^k + \delta_2\left(b^{k+1} - L_C X^{k+1}\right) \end{aligned} \tag{18}$$

where δ_1 and δ_2 are the update sizes for the iteration. The primal problem of Eq. (18) can be solved by optimizing X, a, and b alternately as follows

$$\begin{aligned} X^{k+1} &= \arg\min \mathcal{L}\left(X, a^k, b^k, u^k, v^k\right) \\ a^{k+1} &= \arg\min \lambda_1 \left\| a \right\|_1 + \langle u^k, a - X^{k+1} \rangle + \frac{\mu_1}{2}\left\| a - X^{k+1} \right\|_2^2 \\ b^{k+1} &= \arg\min \lambda_2 \left\| b \right\|_1 + \langle v^k, b - L_C X^{K+1} \rangle \\ &\quad + \frac{\mu_2}{2}\left\| b - L_C X^{k+1} \right\|_2^2 \end{aligned} \tag{19}$$

Therefore, the complete procedure of the GWNFL method for NIR-II/NIR-I FMT is summarized in Algorithm 1. The reconstruction algorithm was implemented using MATLAB (2017a) on a desktop computer with Intel(R) Core(TM) i7-6700 CPU (3.40 GHz) and 16GB RAM.

Algorithm 1 Solving NIR-II/NIR-I FMT by GWNFL

Input: Obtain the measured emission light distribution Φ_m^s and the corresponding system matrix A^s.
Step 1: Set the neighbor number k and calculate the Gaussian weights by Eq. (10).
Step 2: Calculate the correlation matrix L_C by Eq. (12) and (13).
Step 3: Set the update size δ_1, δ_2 and initialize the iteration variables X^0, a^0, b^0, u^0, v^0.
Repeat
Step 4: Update X. $X^{k+1} = \arg\min \mathcal{L}\left(X, a^k, b^k, u^k, v^k\right)$.
Step 5: Update a. $a^{k+1} = \arg\min \lambda_1 \left\| a \right\|_1 + \langle u_k, a - X^{k+1} \rangle + \frac{\mu_1}{2}\left\| a - X^{k+1} \right\|_2^2$.
Step 6: Update b. $b^{k+1} = \arg\min \lambda_2 \left\| b \right\|_1 + \langle v_k, b - L_C X^{k+1} \rangle + \frac{\mu_2}{2}\left\| b - L_C X^{k+1} \right\|_2^2$.
Step 7: Update u. $u^{k+1} = u^k + \delta_1\left(a^{k+1} - X^{k+1}\right)$
Step 8: Update v.$v^{k+1} = v^k + \delta_2\left(b^{k+1} - L_c X^{k+1}\right)$
Until stopping criterion is met.
Output: $X = X^*$

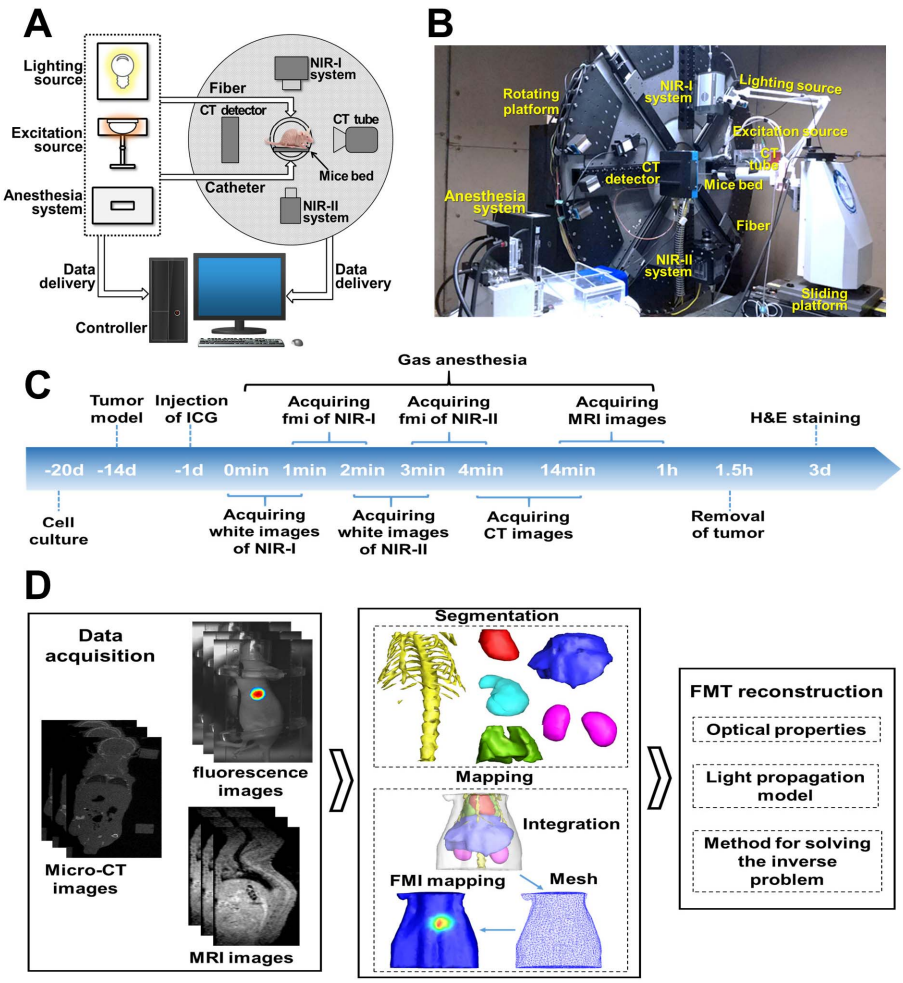

Fig. 2. Imaging system and operation procedure for *in vivo* experiment. (A) The schematic diagram of the imaging system. (B) Photograph of the overview of the system was taken beside the rotating gantry. (C) Workflow of *in vivo* NIR-II /NIR-I dual-modal imaging is shown with imaging events. Time points begins from starting of acquiring white images of NIR-I. (D) Reconstruction workflow of NIR-II/NIR-I FMT, including three main steps: data acquisition, data process and FMT reconstruction.

D. In Vivo Experiments

1) NIR-II/NIR-I Dual-Modality FMT System: A novel NIR-II/NIR-I dual-modality FMT system was constructed for *in vivo* NIR-II FMT and NIR-I FMT simultaneously (Fig. 2A). The signal acquisition modules of this system can obtain NIR-II fluorescence images, NIR-I fluorescence images and CT images successively, which was integrated on the rotating platform. Auxiliary imaging modules including a lighting source, an excitation source, and an anesthesia system were laid aside the rotating platform [40], [41]. To acquire the CT signal, an X-ray tube (L9181002X, Hamamatsu Photonics, Japan) and the corresponding CMOS X-ray detector (C7942CA-22, Hamamatsu, Japan) were arranged at the horizontal direction of the rotating platform (Fig. 2B). A high sensitivity InGaAs charge-coupled device camera (NIRvana 640, Princeton Instruments, USA) coupled to a C-mount lens (SWIRON 2.8/50, Schneider, France) was situated on the top direction to obtain the NIR-II FMI signal. For NIR-I FMI, an electron-multiplying charge-coupled device (EMCCD, iKon-M 934, Andor, UK) camera was coupled to a lens (M3514-SW, Computar, USA) and fixed on the bottom direction. The 808 nm laser (output power 2W, MW-GX-808, Changchun Reirui Optoelectronic Technology, China) and the NIR lamp were used as the excitation source and lighting source, respectively. The excitation equipment included the laser, optical fiber, and beam expander. A gas anesthesia system was used on the experiment mice on the mice bed. The catheter is a thin flexible tube to permit introduction of anesthetic gas.

2) Procedure of In Vivo Experiments: All *in vivo* animal experiments were approved by the Institutional Animal Care and Use Committee, Chinese Academy of Sciences. All the procedures were conducted in strict accordance with the appropriate institutional guidelines and animal ethics for animal research. The whole procedure of the *in vivo* NIR-II/NIR-I FMT experiments was showed in Fig. 2C. To establish the tumor models for NIR-II/NIR-I FMT, the five-week-old female BALB/c nude mice (n = 4) weighed 15-20g were purchased from Vital River Laboratory Animal Technology Co., Ltd., Beijing, China. About 1×10^7 HepG2-Red-Fluc cells were implanted subcutaneously in the left front flank of each mouse. Two weeks later, the subcutaneous tumors reached ~8 mm in diameter and the HepG2 tumor-bearing mice (n = 4) were injected with ICG

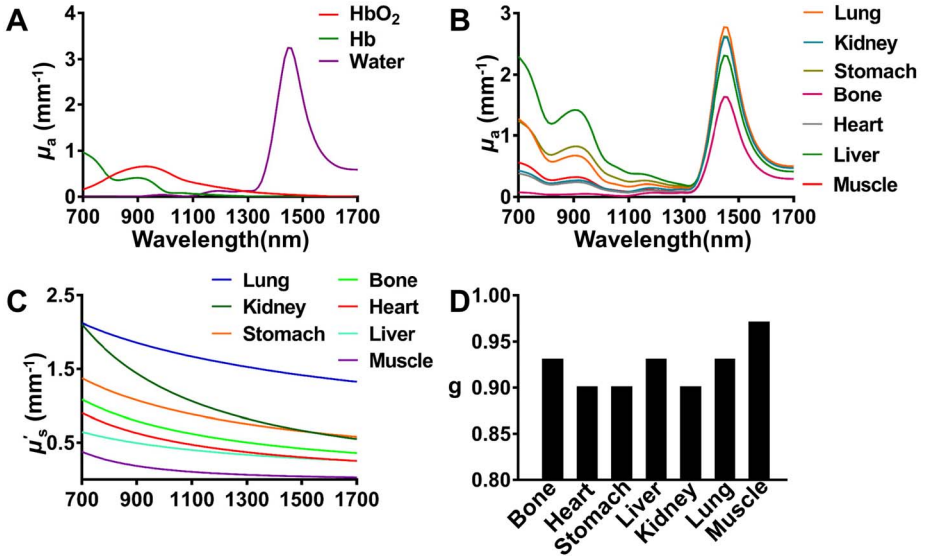

Fig. 3. The optical properties of light in the NIR-II/NIR-I region (700-1700 nm). (A) The absorption spectrum of three main components in the biological tissues. (B) The absorption spectrum of seven organs. (C) The reduced scattering coefficients. (D) The anisotropic coefficients.

(0.1 mg/ml, 0.1 ml) via the tail vein. 24h later, FMI experiments were conducted with the tumor-bearing mice under the condition of gas anesthesia with 2% isoflurane. NIR-II FMI, NIR-I FMI, and CT were acquired successively after the InGaAs CCD camera and the EMCCD camera was cooled to -80° to reduce the thermal noise. The near-infrared lamp was turned on to acquire the NIR-II white light images, which were used to locate the marker points for the purpose of optical image and 3D shape co-registration.

The fluorescence images were subject to background subtraction and flat field correction in the acquisition software. For each mouse, eight angular steps were used in the tomography acquisition. Then, each mouse was imaged via MRI (1.5T, M3TM, Aspect Imaging, Israel) for the verification of tumors location and shape. Finally, the hematoxylin and eosin (H&E) stain were performed to verify that the implanted mass is indeed a tumor. NIR-II/NIR-I FMT were performed after acquiring the optical images and CT structural images with GWNFL method (Fig. 2D). Firstly, the major organs were segmented from the 3D volume data with MITK Workbench 2016.11.0 and then integrated into *in vivo* mouse model. The mouse mesh was generated with Amira 5.4 and the tumor signal in the fluorescence image was mapped to the mouse mesh to generate the photon distribution on the 3D surface (Φ_m^s) through the marker points. Finally, the system matrix (A^s) was calculated and the inverse problem was solved by GWNFL method.

E. Evaluation Index

To compare the positioning accuracy of NIR-II FMT and NIR-I FMT, location error (LE) was adopted in this study. LE is the Euclidean distance between the reconstructed center and the real tumor center as:

$$LE = \|R - T\|_2 = \sqrt{(x - x_0)^2 + (y - y_0)^2 + (z - z_0)^2} \tag{20}$$

where $R = (x, y, z)$ is the reconstructed source center and $T = (x_0, y_0, z_0)$ is the true tumor center. Dice index is employed to access the spatial overlap performance of the reconstructed source and the true source:

$$Dice = \frac{2\,|X \cap Y|}{|X| + |Y|} \tag{21}$$

where X and Y are the reconstructed and actual area, respectively. The value of Dice index ranges from 0 to 1. Relative intensity error (RIE) was adopted to evaluate the intensity deviation between the reconstructed source intensity I and the real source intensity I_0 as follows:

$$RIE = \frac{|I - I_0|}{I_0} \times 100\% \tag{22}$$

Furhter, all statistical analysis results were visualized with GraphPad Prism 7.00.

III. Results

A. Optical Properties

The optical properties of different biological tissues are essential to establish the light propagation model for NIR-II FMT. Seven major abdominal tissues used for FMT were taken into consideration, including bone, heart, kidney, liver, lung, muscle and stomach. The absorption effect of oxy-hemoglobin, hypoxic hemoglobin was predominant in the shorter wavelength region (700-1300 nm) (Fig. 3A). When the wavelength was greater than 1300 nm, the absorption effect increased rapidly and reached its peak at ~1450 nm. There was a rough downward trend for the absorption coefficients of all tissues when the wavelength increased from 700 nm to 1300 nm (Fig. 3B). However, the absorption coefficient ascended quickly when the wavelength was larger than 1300 nm. In addition, there existed obvious difference between absorption coefficients of biological tissues. All reduced scattering coefficients of seven biological tissues

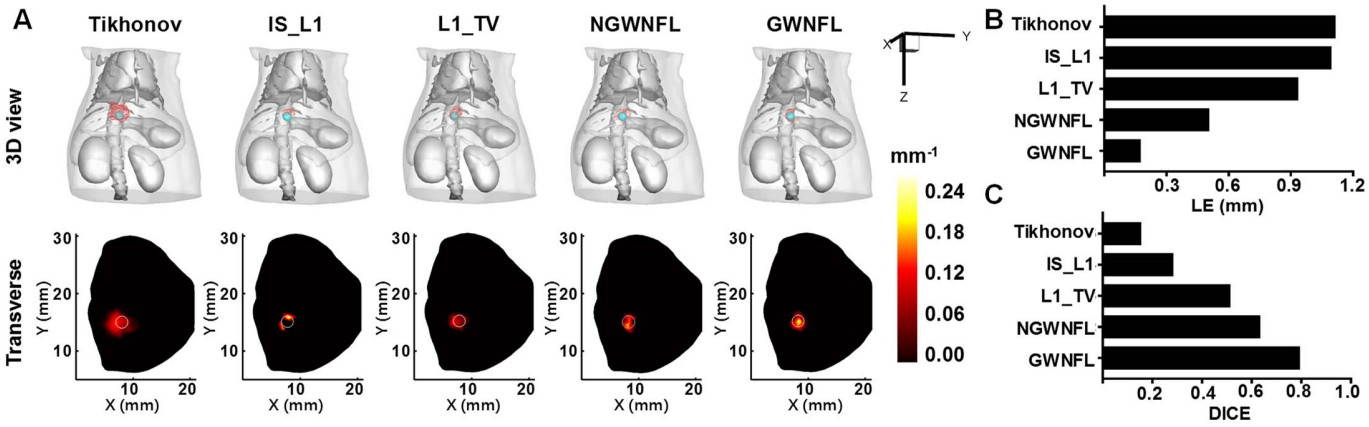

Fig. 4. Results of GWNFL's performance comparison. (A) NIR-II FMT reconstruction results using different approaches. Both 3D view and transverse slice view are presented for comparisons. Blue spheres and white cycles denote the ground truth of the sources in 3D view and axial slice view. (B) and (C) show the quantitative analysis of LE and Dice, respectively.

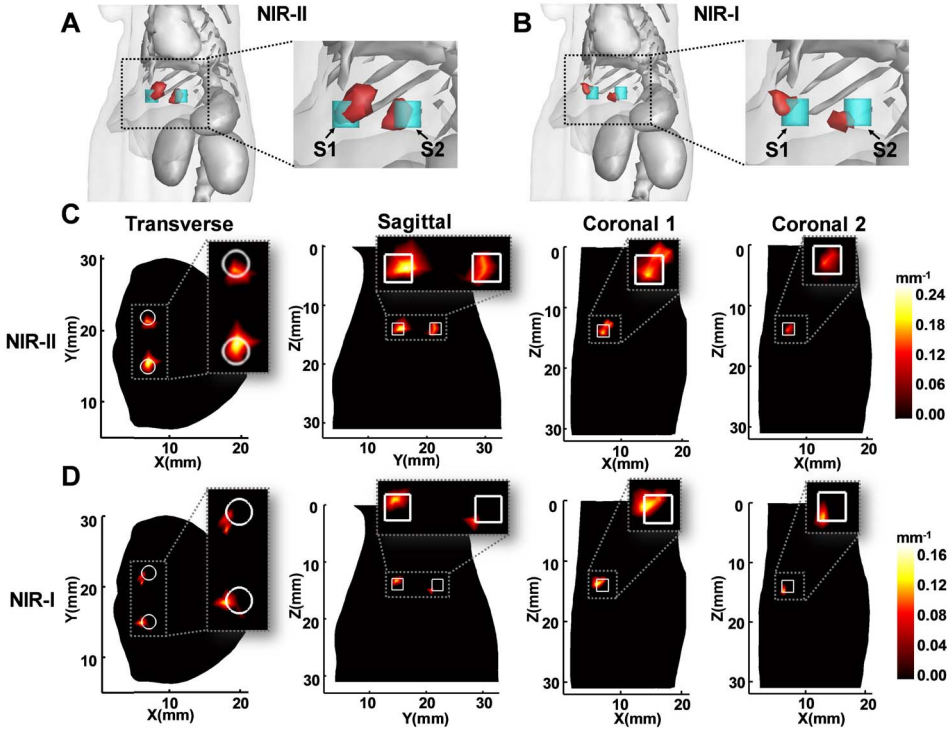

Fig. 5. Results of the reconstruction accuracy verification simulation. (A-B) The reconstruction results of NIR-II/NIR-I FMT in 3D view. (C-D) The reconstruction results of NIR-II/NIR-I FMT in transverse view, sagittal view and coronal view.

decreased with the increase in the wavelength (Fig. 3C). Lastly, there was a small difference in anisotropy coefficients between different tissues (Fig. 3D).

To investigate the different penetration and resolution abilities of the NIR-II/NIR-I light based on the optical properties, the photon propagation simulation was provided in the Supplemental Materials Section S. I.

B. GWNFL's Performance Comparison

To verify the reconstruction performance of GWNFL, a NIR-II FMT reconstruction numerical simulation was conducted, since GWNFL method was independent of the wavelength regime. A spherical source with a radius of 1 mm was implanted in the digital mouse at point (8, 15, 14) mm. 10% Gaussian noise was added to the surface flux signals. Tikhonov, IS_L1, L1_TV and NGWNFL were used for comparison.

Fig. 4 presents the reconstruction results of five methods. The true source and reconstructed source were displayed in 3D and transverse views (Fig. 4A). The quantitative analysis of LE and Dice were shown in Fig. 4B and C. GWNFL method achieved most accurate reconstruction results with least LE of 0.17 mm and highest Dice of 0.79. The results showed GWNFL method obtained a more accurate solution of the inverse problem, which was the solid foundation for NIR-II/NIR-I reconstruction.

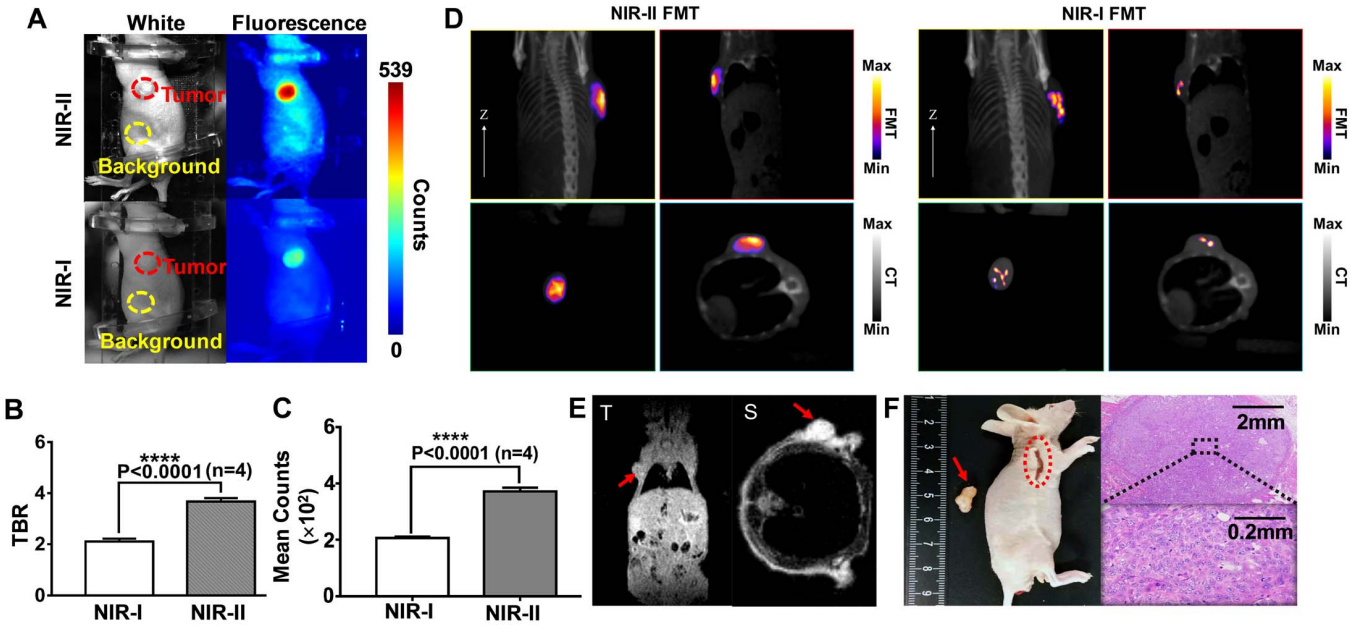

Fig. 6. The *in vivo* reconstruction results. (A) White light images and fluorescence images of NIR-II and NIR-I are shown irrespectively. (B) The TBR of NIR-II/NIR-I FMI. (C) The NIR-II/NIR-I fluorescence signal intensity. (D) The results of NIR-II FMT and NIR-I FMT are shown irrespectively in the 3D maximum intensity projection view, coronal view and sagittal view and the transversal view. (E) The transversal view and sagittal view of the corresponding MRI slices. (F) The subcutaneous tumor and its H&E stain images.

TABLE I
QUANTITATIVE RESULTS FOR NUMERICAL SIMULATION

Method	True (mm)	Results (mm)	LE (mm)	Dice	RIE
NIR-II	S1 (7, 15, 14)	(7.1, 14.8, 13.4)	0.65	0.75	19.1%
	S2 (7, 22, 14)	(6.8, 21.8, 14.2)	0.36	0.50	31.4%
	Total	/	1.01	0.58	/
NIR-I	S1 (7, 15, 14)	(6.2, 14.6, 13.2)	1.17	0.40	44.2%
	S2 (7, 22, 14)	(6.1, 21.3, 14.3)	1.20	0.13	62.5%
	Total	/	2.37	0.19	/

C. Reconstruction Accuracy Verification

A reconstruction numerical simulation was conducted to verify the reconstruction effects of NIR-II FMT, and it was compared with that of the traditional NIR-I FMT. The reconstruction results were displayed in 3D view and slice views. In the 3D view, the blue cylinders and the red area represented the real fluorescent sources and the reconstructed fluorescent source region (Fig. 5A-B). The zoom-in view beside the 3D view provided a closer look at the distributions of the reconstructed area. The reconstruction results were also shown in transverse, sagittal, and coronal slice views (Fig. 5C-D). The white edges denoted the real fluorescent sources and the color areas represented the reconstructed sources. Local enlarged images were displayed at the top-right corner of the original images to have a clear look at the reconstructed sources. The qualitative comparison demonstrated that the reconstruction results of NIR-II FMT were more similar to the true sources than that of NIR-I FMT.

The same results were also observed by the quantitative comparisons of the reconstruction results that were implemented with LE, Dice and RIE, which were summarized in Table I. The LE of NIR-II FMT for S1, S2 and total was only 0.65 mm, 0.36 mm and 1.01 mm respectively, which is much lower than the LE of NIR-I FMT with 1.17 mm, 1.20 mm and 2.37 mm. Further, the reconstruction results of NIR-II FMT obtained much larger Dice. The Dice of NIR-II were 0.75, 0.50, and 0.58 and that of NIR-I FMT were 0.40, 0.13, and 0.19. According to the Dice, the level of similarity of NIR-II FMT was about 2 to 3 times more than that of NIR-I FMT. Lastly, it was found that the RIEs of NIR-II FMT were 19.1% and 31.4%, much smaller than NIR-I FMT. The results of comparison demonstrated that NIR-II FMT had a much better effect in the source location, spatial overlap, and relative intensity.

D. In Vivo Reconstruction

To assess the reconstruction effects of NIR-II FMT and NIR-I FMT, the *in vivo* experiment was performed to detect the subcutaneous transplanted liver tumors of mice. The represented reconstruction results of one mouse among four mice were illustrated (Fig. 6). The planar results including white light images and fluorescence images were achieved successively (Fig. 6A). The comparison results of fluorescence images showed that tumor-background-ratio (TBR) and fluorescent signal intensity of NIR-II FMI were both significantly higher than NIR-I FMI (Fig. 6B-C). Then, the reconstruction results of NIR-II/NIR-I FMT were achieved and merged with the CT images (Fig. 6D). The CT images provided the

TABLE II
QUANTITATIVE RESULTS FOR *in vivo* EXPERIMENTS

Method	LE (mm)	Dice
NIR-II FMT	0.84	0.76
NIR-I FMT	2.13	0.22

structural signal at a high resolution and topology. In each subfigure, the reconstruction results were displayed in the 3D maximum intensity projection view (M), the coronal view (C), the sagittal view (S) and the transversal view (T). The actual tumor area was extracted from the MRI images as shown by the red arrows in (S) and (T) view (Fig. 6E). It was evident that the reconstructed tumor area of NIR-II FMT was closer to the actual area depicted by MRI images than that of NIR-I FMT. The quantitative comparison results of *in vivo* reconstruction were displayed in Table II. In terms of tumor location, the location error of NIR-I FMT and NIR-II FMT were 2.13 mm and 0.84 mm, respectively. The Dice similarity coefficients between the reconstructed area and the actual area were 0.76 for NIR-II FMT and 0.22 for NIR-I FMT. Overall, comparison results of *in vivo* reconstruction clearly revealed a better performance of NIR-II FMT in terms of location accuracy and spatial overlap. Lastly, Fig. 6F illustrated the photograph of the resected tumor and the H&E staining images in 40X and 400X magnification view. The H&E results showed that the reconstruction area was the real cancer tissue. All these data demonstrated the NIR-II FMT had satisfactory reconstruction results for *in vivo* tumor detection.

Since the subcutaneous tumor is superficial, being unable to assess the performance thoroughly, we conducted deeper fluorescence source experiments using the homogeneous phantom and heterogeneous mice. More details were illustrated in Supplementary Materials Section S.II.

IV. DISCUSSION AND CONCLUSION

FMT can be used to display the 3D spatial distribution of fluorescence probes concentrated in the imaging targets such as tumors, organs, blood vessels and other tissues in living animals. However, because of the strong scattering and absorption effect of NIR-I light, the reconstruction performance of the traditional NIR-I FMT remains unsatisfactory for its high ill-posedness. It is significant to further improve the reconstruction performance to promote the application of FMT in preclinical and clinical researches. Theoretical and experimental studies show that the performance of FMT is closely related to the light scattering and absorption effect of biological tissues. In recent years, with the development of novel imaging dyes and CCDs, considerable research attention has been paid to FMI in the NIR-II region for its lower scattering and absorption caused by the longer wavelength. Given the above, FMT has been expanded to the NIR-II region on a heterogeneous mouse model in this study. Accordingly, there are three main problems that need to be solved in the process of NIR-II FMT: 1) the NIR-II optical properties of different biological tissues; 2) the NIR-II FMT system for acquiring structural images and fluorescence imaging of small animals; and 3) the regularization method to solve the inverse problem of NIR-II FMT. We focused on the solution of these problems in this paper and demonstrate that NIR-II FMT has better performance than NIR-I FMT.

The optical properties of different biological tissues in the NIR-II/NIR-I region are analyzed by empirical formulas shown in Eq. (6) and (7) according to previous studies. Therefore, these optical properties may deviate from the actual value and a further study can be attempted to measure the optical properties by experimental methods. Two shorter NIR-II wavelengths (1100 nm and 1300 nm) were selected to validate the penetration and resolution abilities compared to the NIR-I wavelength (800 nm) by Monte Carlo method. The attributes of light at different wavelengths were compared by eliminating experimental factors such as experimental system, experimental setup, and so on, which provided a new idea to compare the performance of FMI under different wavelengths.

In this study, we proposed NIR-II FMT, attempting to improve FMT reconstruction performance from the perspective of photon propagation model (reduction in absorption and scattering of most biological tissues). On this basis, we presented GWNFL method to solve the inverse problem accurately from the perspective of model solution (a Gaussian weighted collection of neighboring nodes in the regularization). GWNFL method obtained a more accurate solution of the inverse problem in FMT reconstruction, independent of the wavelength regime. It was modified from the fused Lasso method by calculating the correlation between a mesh node and its k-nearest neighbors. The Gaussian distance was used to evaluate the correlation and the objective function was solved by the split Bregman method. Algorithm comparison simulation proves the advantage of the proposed GWNFL method compared with other methods. Although GWNFL method performed well both in NIR-II FMT and NIR-I FMT, it can be further improved by adding more local information such as node energy, element connectivity or even voxel correlation. Further, it is significant for NIR-II/NIR-I FMT to find the regularization parameter adaptively. A novel NIR-II/NIR-I dual-modality FMT system was established to compare the reconstruction performance of NIR-II/NIR-I FMT for *in vivo* experiments. This system acquires CT images, NIR-I images and NIR-II images successively, which provides bi-spectra FMT for imaging two different biological tissues simultaneously.

The reconstruction performance of NIR-II/NIR-I FMT was compared by numerical simulations and *in vivo* experiments. In dual-source numerical simulation, the location accuracy and spatial overlap were evaluated. Compared with traditional NIR-I FMT, NIR-II FMT significantly reduce the location error by 57.46%. The dice coefficient of NIR-II FMT is increased by 2 to 3 times than NIR-I FMT, indicating that the spatial overlap ability has been greatly improved. In the *in vivo* experiment, the reconstructed tumor area of NIR-II FMT is more similar to the real tumor in terms of location and shape. The favorable penetration and resolution abilities of NIR-II light alleviate the crosstalk among different sources and reduce the noise influence, which may improve the reconstruction performance greatly. The *in vivo* NIR-I results are very different from the NIR-II results in terms of sparsity and noise, mainly

due to the different optical properties between the NIR-I light and NIR-II light and their different interaction properties with biological tissues. The application of NIR-II FMT deserves further exploration such as the detection of deeper tissues and multiple-source resolution.

In conclusion, the NIR-II FMT of heterogeneous mice by GWNFL method was developed in this study, and the performance was compared with that of NIR-I FMT. The results of the numerical simulations and *in vivo* experiments both demonstrated the better reconstruction performance of NIR-II FMT in terms of location accuracy and spatial overlap. This study will benefit the development and application of the NIR-II FMT in the future.

ACKNOWLEDGMENT

The authors would like to thank J. Yang and H. Guo for the assistance of *in vivo* experiments.

REFERENCES

[1] X. Michalet, "Quantum dots for live cells, *in vivo* imaging, and diagnostics," *Science*, vol. 307, no. 5709, pp. 538–544, Jan. 2005.

[2] Z. Hu *et al.*, "*In vivo* nanoparticle-mediated radiopharmaceutical-excited fluorescence molecular imaging," *Nature Commun.*, vol. 6, Jun. 2015, Art. no. 7560.

[3] X. Gao, Y. Cui, R. M. Levenson, L. W. K. Chung, and S. Nie, "*In vivo* cancer targeting and imaging with semiconductor quantum dots," *Nature Biotechnol.*, vol. 22, no. 8, pp. 969–976, Aug. 2004.

[4] C. Wang *et al.*, "Optical molecular imaging for tumor detection and image-guided surgery," *Biomaterials*, vol. 157, pp. 62–75, Mar. 2018.

[5] V. Ntziachristos, "Fluorescence molecular imaging," *Annu. Rev. Biomed. Eng.*, vol. 8, pp. 1–33, Aug. 2006.

[6] R. T. Sadikot and T. S. Blackwell, "Bioluminescence imaging," *Proc. Amer. Thoracic Soc.*, vol. 2, no. 6, pp. 537–540, 2005.

[7] E. Ciarrocchi and N. Belcari, "Cerenkov luminescence imaging: Physics principles and potential applications in biomedical sciences," *Esther Ciarrocchi*, vol. 4, no. 1, 2017, Art. no. 14.

[8] Y. An *et al.*, "A novel region reconstruction method for fluorescence molecular tomography," *IEEE Trans. Biomed. Eng.*, vol. 62, no. 7, pp. 1818–1826, Jul. 2015.

[9] S. Jiang *et al.*, "Novel $l_{2,1}$-norm optimization method for fluorescence molecular tomography reconstruction," *Biomed. Opt. Express*, vol. 7, no. 6, pp. 2342–2359, Jun. 2016.

[10] A. Ale, V. Ermolayev, E. Herzog, C. Cohrs, M. H. De Angelis, and V. Ntziachristos, "FMT-XCT: *In vivo* animal studies with hybrid fluorescence molecular tomography–X-ray computed tomography," *Nature Methods*, vol. 9, no. 6, pp. 615–620, Jun. 2012.

[11] F. Stuker *et al.*, "Hybrid small animal imaging system combining magnetic resonance imaging with fluorescence tomography using single photon avalanche diode detectors," *IEEE Trans. Med. Imag.*, vol. 30, no. 6, pp. 1265–1273, Jun. 2011.

[12] S. Zhang *et al.*, "Robust reconstruction of fluorescence molecular tomography based on sparsity adaptive correntropy matching pursuit method for stem cell distribution," *IEEE Trans. Med. Imag.*, vol. 37, no. 10, pp. 2176–2184, Oct. 2018.

[13] X. Guo *et al.*, "A combined fluorescence and microcomputed tomography system for small animal imaging," *IEEE Trans. Biomed. Eng.*, vol. 57, no. 12, pp. 2876–2883, Dec. 2010.

[14] P. Mohajerani and V. Ntziachristos, "An inversion scheme for hybrid fluorescence molecular tomography using a fuzzy inference system," *IEEE Trans. Med. Imag.*, vol. 35, no. 2, pp. 381–390, Feb. 2016.

[15] T. Lasser, A. Soubret, J. Ripoll, and V. Ntziachristos, "Surface reconstruction for free-space 360° fluorescence molecular tomography and the effects of animal motion," *IEEE Trans. Med. Imag.*, vol. 27, no. 2, pp. 188–194, Feb. 2008.

[16] J. Zhang *et al.*, "Iterative correction scheme based on discrete cosine transform and L1 regularization for fluorescence molecular tomography with background fluorescence," *IEEE Trans. Biomed. Eng.*, vol. 63, no. 6, pp. 1107–1115, Jun. 2016.

[17] H. Yi *et al.*, "Reconstruction algorithms based on l1-norm and l2-norm for two imaging models of fluorescence molecular tomography: A comparative study," *J. Biomed. Opt*, vol. 18, no. 5, May 2013, Art. no. 056013.

[18] D. Zhu and C. Li, "Nonconvex regularizations in fluorescence molecular tomography for sparsity enhancement," *Phys. Med. Biol.*, vol. 59, no. 12, pp. 2901–2912, Jun. 2014.

[19] J. Dutta, S. Ahn, C. Li, S. R. Cherry, and R. M. Leahy, "Joint L1 and total variation regularization for fluorescence molecular tomography," *Phys. Med. Biol.*, vol. 57, no. 6, pp. 1459–1476, 2012.

[20] M. J. Niedre, R. H. De Kleine, E. Aikawa, D. G. Kirsch, R. Weissleder, and V. Ntziachristos, "Early photon tomography allows fluorescence detection of lung carcinomas and disease progression in mice *in vivo*," *Proc. Nat. Acad. Sci. USA*, vol. 105, no. 49, pp. 19126–19131, Dec. 2008.

[21] G. Hong, S. Diao, A. L. Antaris, and H. Dai, "Carbon nanomaterials for biological imaging and nanomedicinal therapy," *Chem. Rev.*, vol. 115, no. 19, pp. 10816–10906, Oct. 2015.

[22] K. Welsher, S. P. Sherlock, and H. Dai, "Deep-tissue anatomical imaging of mice using carbon nanotube fluorophores in the second near-infrared window," *Proc. Nat. Acad. Sci. USA*, vol. 108, no. 22, pp. 8943–8948, May 2011.

[23] G. Hong *et al.*, "Multifunctional *in vivo* vascular imaging using near-infrared II fluorescence," *Nature Med.*, vol. 18, no. 12, pp. 1841–1846, Dec. 2012.

[24] A. L. Antaris *et al.*, "A small-molecule dye for NIR-II imaging," *Nature Mater.*, vol. 15, no. 2, pp. 235–242, Feb. 2016.

[25] G. Hong, A. L. Antaris, and H. Dai, "Near-infrared fluorophores for biomedical imaging," *Nature Biomed. Eng.*, vol. 1, no. 1, Jan. 2017, Art. no. 0010.

[26] J. A. Carr *et al.*, "Shortwave infrared fluorescence imaging with the clinically approved near-infrared dye indocyanine green," *Proc. Nat. Acad. Sci. USA*, vol. 115, no. 17, pp. 4465–4470, Apr. 2018.

[27] Z. Starosolski, R. Bhavane, K. B. Ghaghada, S. A. Vasudevan, A. Kaay, and A. Annapragada, "Indocyanine green fluorescence in second near-infrared (NIR-II) window," *PLoS ONE*, vol. 12, no. 11, Nov. 2017, Art. no. e0187563.

[28] A. L. Antaris *et al.*, "A high quantum yield molecule-protein complex fluorophore for near-infrared II imaging," *Nature Commun.*, vol. 8, May 2017, Art. no. 15269.

[29] K. Wang, Q. Wang, Q. Luo, and X. Yang, "Fluorescence molecular tomography in the second near-infrared window," *Opt. Express*, vol. 23, no. 10, pp. 12669–12679, May 2015.

[30] J. H. Lee, A. Joshi, and E. M. Sevick-Muraca, "Fully adaptive finite element based tomography using tetrahedral dual-meshing for fluorescence enhanced optical imaging in tissue," *Opt. Express*, vol. 15, no. 11, pp. 6955–6975, May 2007.

[31] G. Alexandrakis, F. R. Rannou, and A. F. Chatziioannou, "Tomographic bioluminescence imaging by use of a combined optical-PET (OPET) system: A computer simulation feasibility study," *Phys. Med. Biol.*, vol. 50, no. 17, pp. 4225–4241, Sep. 2005.

[32] R. P. Brown, M. D. Delp, S. L. Lindstedt, L. R. Rhomberg, and R. P. Beliles, "Physiological parameter values for physiologically based pharmacokinetic models," *Toxicol. Ind. Health*, vol. 13, no. 4, pp. 407–484, Jul. 1997.

[33] K. F. Palmer and D. Williams, "Optical properties of water in the near infrared," *J. Opt. Soc. Amer.*, vol. 64, no. 8, pp. 1107–1110, 1974.

[34] W. Cheong, S. Prahl, and A. Welch, "A review of the optical properties of biological tissues," *IEEE J. Quantum Electron.*, vol. 26, no. 12, pp. 2166–2185, Dec. 1990.

[35] S. L. Jacques, "Optical properties of biological tissues: A review," *Phys. Med. Biol.*, vol. 58, no. 11, pp. R37–R61, Jun. 2013.

[36] S. Jiang *et al.*, "Reconstruction of fluorescence molecular tomography via a fused LASSO method based on group sparsity prior," *IEEE Trans. Biomed. Eng.*, vol. 66, no. 5, pp. 1361–1371, May 2019.

[37] G.-B. Ye and X. Xie, "Split Bregman method for large scale fused Lasso," *Comput. Statist. Data Anal.*, vol. 55, no. 4, pp. 1552–1569, Apr. 2011.

[38] T. Goldstein and S. Osher, "The split Bregman method for L1-regularized problems," *SIAM J. Imag. Sci.*, vol. 2, no. 2, pp. 323–343, Jan. 2009.

[39] J. Zou and Y. Fu, "Split Bregman algorithms for sparse group Lasso with application to MRI reconstruction," *Multidimensional Syst. Signal Process.*, vol. 26, no. 3, pp. 787–802, Jul. 2015.

[40] M. Liu *et al.*, "*In vivo* pentamodal tomographic imaging for small animals," *Biomed. Opt. Express*, vol. 8, no. 3, pp. 1356–1371, Mar. 2017.

[41] T. Song *et al.*, "A novel endoscopic cerenkov luminescence imaging system for intraoperative surgical navigation," *Mol. Imag.*, vol. 14, no. 8, Aug. 2015, Art. no. 7290.2015.